Journal of Materials Chemistry A

PAPER

View Article Online
View Journal | View Issue

Cite this: J. Mater. Chem. A, 2019, 7, 19984

Stability of push–pull small molecule donors for organic photovoltaics: spectroscopic degradation of acceptor endcaps on benzo[1,2-*b*:4,5-*b*′] dithiophene cores†

Kristen E. Watts, ‡[a] Trung Nguyen,‡[b] Bertrand J. Tremolet de Villers,[c] Bharati Neelamraju,[b] Michael A. Anderson,[b] Wade A. Braunecker,[c] Andrew J. Ferguson,[c] Ross E. Larsen,[d] Bryon W. Larson,[c] Zbyslaw R. Owczarczyk,[c] Jason R. Pfeilsticker,[c] Jeanne E. Pemberton *[a] and Erin L. Ratcliff *[be]

High efficiency organic photovoltaic devices have relied on the development of new donor and acceptor materials to optimize opto-electronic properties, promote free carrier generation, and suppress recombination losses. With single junction efficiencies exceeding 15%, materials development must now target long-term stability. This work focuses on the photobleaching dynamics and degradation chemistries of a class of small molecule donors inspired by benzodithiophene terthiophene cores (BDT-3T) with rhodanine endcaps, which have demonstrated 9% efficiency in single junction devices and >11% in ternary cells. Density functional theory was used to design three additional molecules with similar synthetic pathways and opto-electronic properties by simply changing the electron accepting endcap to benzothiazoleacetonitrile, pyrazolone, or barbituric acid functional groups. This new class of semiconductors with equivalent redox properties enables systematic investigation into photobleaching dynamics under white light illumination in air. Degradation chemistries are assessed *via* unique spectroscopic signatures for the BDT-3T cores and the endcaps using photoelectron spectroscopies. We show that the pyrazolone undergoes significant degradation due to ring opening, resulting in complete bleaching of the chromophore. The barbituric and rhodanine endcap molecules have moderate stability, while the benzothiazoleacetonitrile group produces the most stable chromophore despite undergoing some oxidative degradation. Collectively, our results suggest the following: (i) degradation is not just dependent on redox properties; (ii) core group stability is not independent of the endcap choice; and (iii) future design of high efficiency materials must consider both photo and chemical stability of the molecule as a whole, not just individual donor or acceptor building blocks.

Received 12th June 2019
Accepted 11th August 2019

DOI: 10.1039/c9ta06310b

rsc.li/materials-a

Introduction

High efficiency organic photovoltaic devices have relied on the development of new donor and acceptor materials to optimize opto-electronic properties. To date, the highest single-junction organic photovoltaic devices have demonstrated >15% power conversion efficiencies (PCE)[1] and reported tandems with PCE ~15–17%.[2,3] Current design guidelines for materials utilize a push–pull concept with alternating electron donating (D) and withdrawing or accepting (A) building blocks, a concept that has been successful for both polymeric and molecular systems. The push–pull concept enables manipulation of the electron density about different parts of the molecule/oligomer for facile tuning of the band gap and redox properties. Such exquisite control over the opto-electronic properties provides opportunity for alternative applications for organic photovoltaic systems, such

[a]Department of Chemistry and Biochemistry, University of Arizona, Tucson, AZ, 85721, USA. E-mail: pembertn@email.arizona.edu

[b]Department of Materials Science and Engineering, University of Arizona, Tucson, AZ, 85721, USA. E-mail: ratcliff@email.arizona.edu

[c]Chemistry and Nanoscience Center, National Renewable Energy Laboratory, Golden, CO, 80401, USA

[d]Computational Science Center, National Renewable Energy Laboratory, Golden, CO, 80401, USA

[e]Department of Chemical and Environmental Engineering, University of Arizona, Tucson, AZ, 85721, USA

† Electronic supplementary information (ESI) available: Synthesis, characterization, additional DFT, UV-Vis, time-dependent FTIR, NEXAFS and XPS data. See DOI: 10.1039/c9ta06310b

‡ Authors contributed equally to this publication.

as integration of photovoltaics in semi-transparent windows, laptop screens, and automobile windshields.[4,5] Of particular note is off-grid deployable OPV coatings for powering greenhouse enclosures, where the opto-electronic properties of the semiconductors can be tuned for maximizing device efficiencies while still retaining transmission of the photosynthetic active radiation.[6]

Many different push–pull materials have been studied in recent years for blended heterojunctions. Generally, the electron donor material in the blended heterojunction has been considered the more photo-unstable component of the blended heterojunction,[7] although fullerene degradation due to dimerization has been reported.[8] Historically, one predominant core unit for donors is the (4,8)alkoxy-substituted benzo[1,2-*b*:4,5-*b*′] dithiophene (BDT) unit, which is a symmetric and coplanar structure that is easily modified with good electron delocalization and high hole mobilities.[9–11] Examples of BDT systems are shown in Chart 1. An early high performing material, termed PTB7 or poly((4,8-bis[(2-ethylhexyl)oxy]benzo[1,2-*b*:4,5-*b*:4,5-*b*′] dithiophene-2,6-diyl)(3-fluoro-2-[(2-ethylhexyl)carbonyl]thieno [3,4-*b*]thiophenediyl)), demonstrated PCE ~7.5% in normal device structures[12] and >9% in an inverted structure with optimized contacts when blended with a fullerene.[13] Photochemical stability of neat polymer and blends with $PC_{70}BM$ found the BDT group to be the site of instability (point of oxidation) and that degradation was accelerated in the presence of the fullerene.[14,15] Structural modification of the PTB7 with alkylthienyl side group pendants (PTB7-Th) advanced PCEs to ~10%, attributed in part to better microstructure control.[16,17] Other strategies to promote photocurrent generation and/or control microstructure during the drying process were attained for the BDT core class of polymers through the use of diiodooctane (DIO) additives.[18,19] Yet degradation continues to be a major problem for these polymers with a perceived catalytic effect of DIO on degradation in microstructure-optimized devices.[20]

More recently, design of blended heterojunction donor materials shifted to highly crystalline oligomers. These "small molecule" (SM) materials are comprised of relatively long conjugation systems (~6 to 10 electron push–pull units) and offer a number of synthetic advantages over polymers: (i) uniform and defined molecular structures to minimize batch-to-batch variations; (ii) higher open circuit voltages; (iii) higher hole mobility; and (iv) structural versatility to enable more refined control of energy levels.[21–23] Additionally, crystalline interactions and formations can be controlled through the molecules themselves, which have the potential to improve long-term stability and reduce processing costs by eliminating the need for additives. One particularly promising class of SMs utilizes BDT with terthiophene spacers (3T),[24] creating a BDT-3T donor′/donor/donor′ core (D′–D–D′) with extended conjugation and a planar structure suggested for high performance OPVs (Chart 1).[25–27] Systematic manipulation of the side chains and endcaps to control liquid crystalline behavior have yielded OPVs with PCE >9% and fill factors as high as 70% (a feature not normally observed in polymeric systems) for the rhodanine endcapped small molecule (SMRh – see Chart 1).[28] A number of derivatives have been synthesized with different endcapped acceptor units, such as side-chain modified rhodanines and thiazolidiones.[29] Further side-chain engineering of the BDT core produced changes in highest molecular orbital levels and charge transport properties,[30–32] reaching above 9.6% PCE for an average of 50 devices for a *meta*-alkylthio side chain.[33]

Importantly, SMs can have unique interactions compared to polymeric analogs, as the extent of delocalization of electron density is confined to a small oligomer unit.[34] Such effects could potentially make the molecules more susceptible to chemical degradation, but, if mechanisms are understood, could also enable design of optimized OSC materials with enhanced stability. For the initial SMRh OPV, Sun *et al.* reported that degradation was still observed in the device, which they attributed to the metal contact.[28] They suggested that the stability is enhanced by switching to SM systems and/or the 3T spacers over the polymeric systems described above; however, no chemical degradation information was provided.

This work focuses on the degradation chemistries of a class of small molecule donors inspired by the highly efficient and commercially available SMRh derivative: rhodanine endcap with alkylthienyl pendants on the BDT-3T core. We focus here strictly on the materials chemistry and eliminate device variables, burn-in loss and degradation effects due to contacts by investigating only the active layer.[35] Our motivation was two-fold: (i) compare molecules with similar synthesis pathways (Knoevenagel condensation) and (ii) limit complications in degradation due to major differences in redox potentials, as singlet oxygen was hypothesized to be the dominant oxidant consistent with prior reports.[36] We thus used DFT to design a class of three additional molecules with similar opto-electronic properties to SMRh, achieved by simply changing the endcap to benzothiazoleacetonitrile (SMCN), pyrazolone (SMPy), or barbituric acid (SMBA) functional groups (Chart 1).

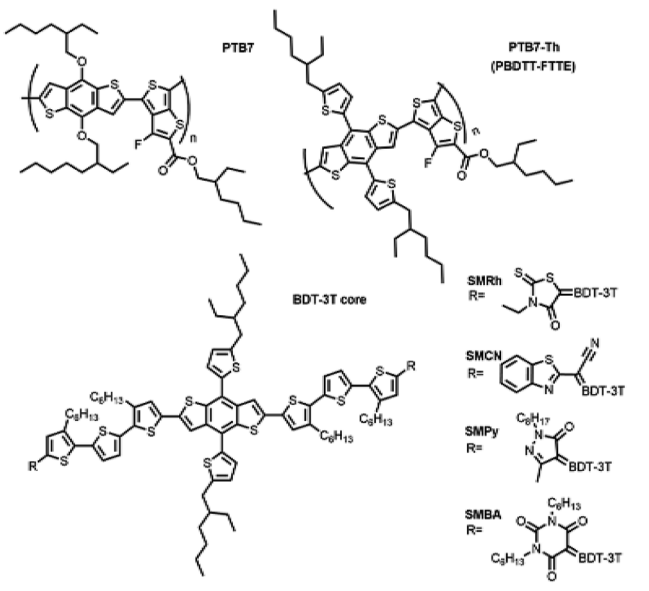

Chart 1 Donor materials for organic solar cells based on benzo[1,2-*b*:4,5-*b*′]dithiophene (BDT) core units, including the molecular system synthesized for photobleaching and chemical degradation studies.

Most critically, each endcap acceptor unit possesses unique spectroscopic signatures independent of the core that can be used to better understand degradation effects. This allows us to evaluate the site of oxidation – *i.e.* the stability of the BDT-3T core as well as the role of the stability of the different endcaps. Time-dependent degradation was monitored using both UV-Vis and FTIR spectroscopies, with changes in optical transmission related to the CIELAB color coordinate system. Changes in frontier orbitals and electronic structure are monitored using a combination of laboratory and synchrotron-based photoelectron spectroscopies. Our results demonstrate the enhanced understanding that can be achieved by using photoelectron spectroscopies to evaluate the local oxidation states of chemical environments for organic push–pull systems and connect molecular-level composition to electronic structure. In particular, we emphasize that photoelectron spectroscopy techniques overcome ambiguity in the FTIR spectral data that results from a combination of spectral congestion and lack of surface sensitivity, and thus, provide detailed evidence for clear changes in spectral signatures days before they are observed by FTIR. Collectively, our results allow the proposal of specific guidelines on designing more stable materials and the need to screen materials independent of full device architectures to elucidate degradation effects, the results of which could be used to engineer efficient encapsulation strategies.

Materials and methods

Synthesis and reagents

All reagents employed in this study were obtained from commercial sources at the highest available purity and used without further purification, unless otherwise noted. Detailed synthesis is provided in the ESI.†. All reactions were performed under dry N_2. THF was purified by passing through alumina in an MBraun solvent purification system. Column chromatography was performed with Fluka Silica Gel 60 (220–440 mesh). Molecules were characterized by ^{1}H NMR (400 MHz) and ^{13}C NMR (100 MHz) on a Bruker Advance III HD NanoBay NMR Spectrometer and using MALDI mass spectrometry using a 7T Fourier transform ion cyclotron resonance mass spectrometer (FT-ICR-MS, SolariX XR, Bruker), with spectra and peaks provided in the ESI section Fig. S1–S10.†

Density functional theory (DFT) calculations

All calculations were performed with the default settings in the Gaussian 09 electronic structure package, revision D.01.[37] The geometric structure of each molecule was optimized in vacuum with the Becke-style three-parameter density functional with the Lee–Yan–Parr correlation function (B3LYP), using the 6-31G(d) basis set. No attempt was made to search through every possible conformer but adjacent thiophene rings were oriented initially in the *trans* configuration with respect to one another. All figures and all quoted electronic properties are for the optimized geometries. For computational efficiency, the alkyl side chains and endcaps were truncated to methyls. We have previously demonstrated that electronic structure of conjugated fused-ring structures is unaffected by replacing a methyl with an ethyl or small branched alkyl such as an isopropyl group.[38]

Time-dependent photobleaching

Photobleaching kinetics were monitored using a previously published approach.[34,39] Briefly, samples were exposed to a four-bulb DC halogen lamp (Sylvania 58321) array providing an output of 120 mW cm^{-2} at the surface of the samples. Radiative heating from the lamps kept the samples at a temperature of 65 °C which was spot-checked throughout the experiments using a contact thermocouple. Ambient conditions and lamp stability were recorded throughout the experiment (see ESI†). Fraction-of-light-absorbed (FA) spectra were calculated using eqn (1) from fraction reflected (FR) and fraction transmitted (FT) spectra collected by separate spectrometers (Ocean Optics HR2000) fitted with a 'six around one' reflectance probe (Ocean Optics R400-7-SR) and a collimating lens respectively.

$$\mathrm{FA} = 1 - \mathrm{FT} - \mathrm{FR} \quad (1)$$

A first surface aluminum mirror was used as the reflectance reference. Accumulated photon dose (t_i) was calculated using eqn (2) where $I_{\mathrm{L,photon}}$ is the spectral photon flux of the degradation lamp array.

$$\text{Photon dose } (t_i) = \int_{t=t_0}^{t=t_i}\int_{\lambda_1}^{\lambda_2} \mathrm{FA}(\lambda, t) \times I_{\mathrm{L,photon}}(\lambda)\mathrm{d}\lambda\mathrm{d}t \quad (2)$$

Spectral irradiance data of the photobleaching light source was gathered using a six-inch integrating sphere (Optronic Labs OL IS-670) fitted with silicon (Soma S-2441C) and InGaAs (Spectral Evolution LF1250) diode arrays. The spectral irradiance data was then converted to photon flux using eqn (3).

$$I_{\mathrm{L,photon}}(\lambda) = \frac{\text{spectral irradiance } (\lambda) \times \lambda}{hc} \quad (3)$$

Photoelectron spectroscopy

X-ray and UV-photoelectron spectroscopy were performed with a Kratos Axis Ultra X-ray photoelectron spectrometer with a monochromatic Al Kα source (1486.6 eV) for XPS measurements and a He(I) excitation source (21.2 eV) for UPS measurements, all at a base pressure of 10^{-9} Torr. Photoelectrons were collected in a hemispherical analyzer and detected with a photodiode array. A −9.00 V bias was applied to the sample to enhance collection of the lowest kinetic energy electrons during UPS analysis. All UPS spectra were referenced to the Fermi level (E_F) of a clean, polycrystalline gold sample. For XPS, a 20 eV pass energy was used for all element specific spectral acquisitions. Resulting XPS spectra were first baseline corrected and then fit using a 40% Gaussian, 60% Lorentzian peak shape. For acquired N 1s spectra, baseline was corrected using a linear subtraction method, and for S 2p spectra a Shirley baseline correction was employed.

Near-edge X-ray absorption fine structure (NEXAFS) spectroscopy

NEXAFS data were acquired at a 55° angle (magic angle) of X-ray incidence using the bending magnet beamline 8-2 at the Stanford Synchrotron Radiation Lightsource (SSRL). Beamline 8-2 is equipped with a spherical grating monochromator, operated using 40 × 40 μm slits corresponding to a resolution of ~0.2 eV. The spot size at the interaction point was around 1 × 1 mm^2 and a flux of 10^{10} photons per s at which beam damage is not noticeable even for extended exposure. The samples were mounted on an aluminum holder using double sided carbon tape, making use of a top mounted manipulator that can be rotated around its own axis, thereby changing the incidence angle of the sample relative to the beam which is highly polarized in the horizontal plane. The magic angle (55° incidence) ensures that any anisotropy in the angular dependence cancels out when azimuthally averaged which is an accurate representation of deposited films on lower symmetry surfaces. The X-ray energies for the S 2p, C 1s, and N 1s edges were scanned from 155 eV to 210 eV, 260 eV to 350 eV, and 380 eV to 440 eV, respectively. Data were collected both in total electron yield (TEY) and Auger Electron Yield (AEY) mode using the drain current (amplified by a Keithley picoammeter) and a Cylindrical Mirror Analyzer (CMA) operated with a pass energy of 200 eV and set to record the main Auger line for the various edges. The incoming flux was recorded using a nickel grid with Au sputtered film. During the time of this experiment, there was some contamination present in the C 1s region, which has been double normalized to reduce the error. However, there remains some uncertainty about the quantification near 285 eV, but this should only have a minor effect on the analysis and does not alter the data interpretation and the main findings. The NEXAFS data was processed using minima offset subtraction and normalizations by the respective intensities at photon energies past the unoccupied sigma peaks. Backgrounds were subtracted using linear background fit functions.

Results and discussion

Opto-electronic properties of the molecular system

In order to guide synthetic design of target molecules with nearly identical opto-electronic properties, we first used density functional theory (DFT) and time-dependent density functional theory (TDDFT) to predict the electronic properties. The output of this simulation was the suggestion for the three small molecules synthesized in this work. Our end goal was to investigate degradation chemistries of the donor materials and thus, we searched for structurally similar molecules with equivalent redox properties (ionization energies and electron affinities). For all three molecules, we truncated each of the alkyl side and end chains to be a methyl functional group. For each optimized geometry, we extracted Kohn–Sham orbital energies of the highest occupied molecular orbital (HOMO) and the lowest unoccupied molecular orbital (LUMO) and several higher-energy unoccupied orbitals ($LUMO^{+1}$, $LUMO^{+2}$, *etc.*) The electronic excitation energies *via* a TDDFT calculation were performed on each optimized geometry. An optical bandgap of ~2.2 eV for each molecule was predicted by DFT. There is general agreement with the measured optical gap using absorbance spectroscopy for each molecule (see Fig. S14†) with an absorption peak at ~2.1 eV for SMRh and ~2.2 eV for SMCN, SMPy, and SMBA. Examples of the contour plots of the HOMO and LUMOs for SMCN are provided in Fig. 1; all others are given in the ESI section (Fig. S11 and S12†).

Each molecule was found to have nearly degenerate LUMO and $LUMO^{+1}$ levels with a small relative energy separation (~80 meV). This near degeneracy is a consequence of the shapes of the LUMO and $LUMO^{+1}$ orbitals; both orbitals consist of wave functions that encompass both the endcaps and the thiophene arms of the molecule. The LUMO orbital consists of a symmetric sum of orbitals from each side (a bonding configuration) and the $LUMO^{+1}$ is an antisymmetric sum of orbitals (an anti-bonding configuration). The small splitting reflects the small overlap at the BDT core between the orbitals from each arm. We anticipate that almost any small molecule consisting of an electron rich core coupled to two arms that have electron poor endcaps will exhibit similar near-degeneracy in the first two unoccupied orbitals, provided the endcaps are sufficiently electron accepting to prevent the LUMO of each arm from spilling appreciably onto the core. We emphasize that the degeneracy of A–D′–D–D′–A systems is unique from the D′–A–D–A–D′ systems,[40–42] which demonstrate a larger split in the LUMO levels due to mixing of the electron density of the acceptor units across the donor core. We hypothesize that the larger separation between the acceptors and the center of the molecule reduces the coupling, leading to the near degeneracy of the systems considered herein.

In organic semiconductors, it is important to consider both the optical and transport levels when constructing devices. Photoelectron spectroscopy is considered the primary tool to evaluate the transport levels in organic semiconductors as it

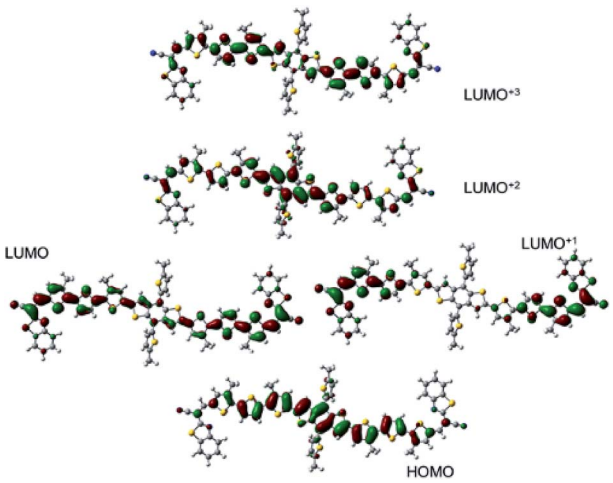

Fig. 1 Contour plots of Kohn–Sham molecular orbitals of SMCN calculated with DFT as described in the text. Displayed are the HOMO, LUMO, $LUMO^{+1}$, $LUMO^{+2}$ and $LUMO^{+3}$ levels for contours at ±0.02 a.u.

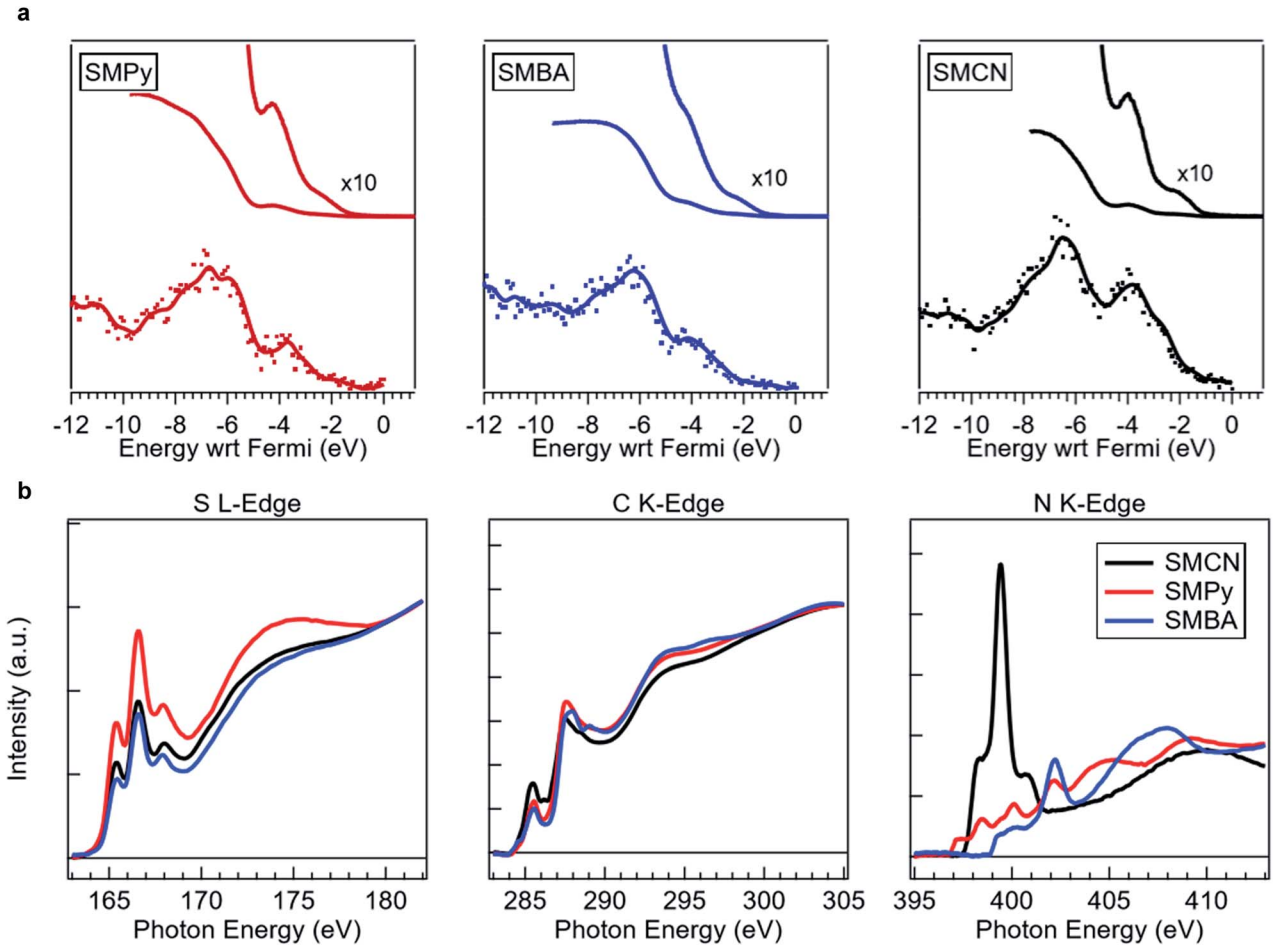

Fig. 2 Photoelectron spectra of occupied and unoccupied molecular orbitals. (a) Valence region collected using He I ultraviolet (top) and monochromatic Al K-α X-ray (bottom) sources and (b) near-edge X-ray absorbance photoelectron spectra of pristine SMPy, SMBA, and SMCN films.

accounts for the initial and final state effects. Specifically, the presence of a carrier on the organic semiconductor results in a polarization of the surrounding molecules accompanied by a nuclear relaxation on the center molecule and is strongly coupled to the intra- and intermolecular vibrations of the solid film. Fig. 2a shows the valence (occupied) structure of each of the three donor molecules (top), using two different photoelectron energies (21.2 and 1486.6 eV), which have different sensitivity factors for different elements. The highest occupied molecular orbital (HOMO) for each molecule was estimated by the onset density of states; each was determined to be ~5.0 eV. DFT confirms that the HOMO of each molecule is located largely on the BDT-3T core and the surrounding thiophene moieties, with minimal electron density associated with the endcaps. The data in Fig. 2a are consistent with the DFT predictions in that the shape of the spectra reflect equivalent elemental contributions.

From the molecular orbitals in Fig. 1, the largest effect of the acceptor endcaps was predicted to be due to LUMO contributions. In order to evaluate the unoccupied states, element-specific near-edge X-ray absorption fine structure (NEXAFS) was used. Fig. 2b shows the overlaid S L-edge (left), C K-edge (center) and N K-edge (right) for the three molecules. The S L-edge is dominated by the BDT-3T core, with very little contribution of the thiazole units for SMCN. The C K-edge shows some change with endcap, indicating that the carbon contributions are impacted by the presence of the endcaps although the spectrum was too congested to identify definitively key features associated strictly with endcaps. In the N K-edge (far right), it is readily apparent that the endcaps have a profound effect on the relative intensities of the core-unoccupied state transitions.

The energy band diagram for each of the three synthesized molecules is shown in Fig. 3 and includes interpretation assisted by DFT. As expected, the neat films all demonstrate similar splitting of unoccupied molecular orbital energies for the first three observable transitions, each on the order of 1–1.5 eV. Collectively, the band diagrams in Fig. 3 clearly demonstrate the ultimate synthetic capability of small molecules to create nearly identical electronic structure derived from unique chemical structures. This is a promising and unique system to use as a testbed to consider degradation moving forwards, as it will enable us to separate out chemical reaction induced degradation from mechanisms associated with energetics and charge carriers.

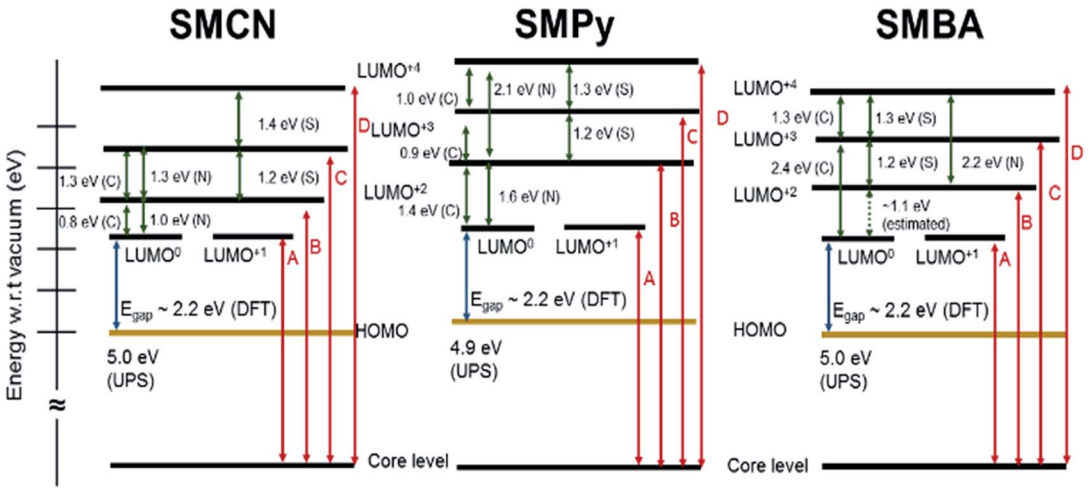

Fig. 3 Energy band diagrams of the three molecules synthesized, incorporating results from UPS, XAS, and DFT. $LUMO^{+x}$ and $LUMO^{+x+1}$ gaps were estimated from different element core transitions specified next to the value.

Time-dependent photobleaching

Thin films of neat donors were aged with continuous ambient illumination and the time-dependent photobleaching was monitored in the visible region. We note that degradation was not observed when stored in ambient under dark conditions nor when light-aged in a glove box. Fig. 4 shows the absorptance spectra of the three synthesized molecules calculated from the transmission and reflection data gathered for 11 days; comparable results for the SMRh molecule are provided in Fig. S15.† The data in Fig. 4 indicate that all molecules exhibit general photobleaching, albeit to varying degrees. Quantification of percent photobleaching is given in Fig. S16.† SMPy exhibits complete photobleaching at 6 days. SMRh and SMBA showed moderate photobleaching initially but bleached by 75% in the 11 day period, while SMCN appears the most stable in terms of opto-electronic properties and retains ~90% of the chromophore after 11 days. We note that the high performing SMRh is not the most stable donor.

In semi-transparent solar window applications for OPVs, either neutral, grey or pure colors are desired and the tolerance for color drift with time is low. Time-dependent absorptance data of the films is plotted in CIE $L^*a^*b^*$ coordinate system in

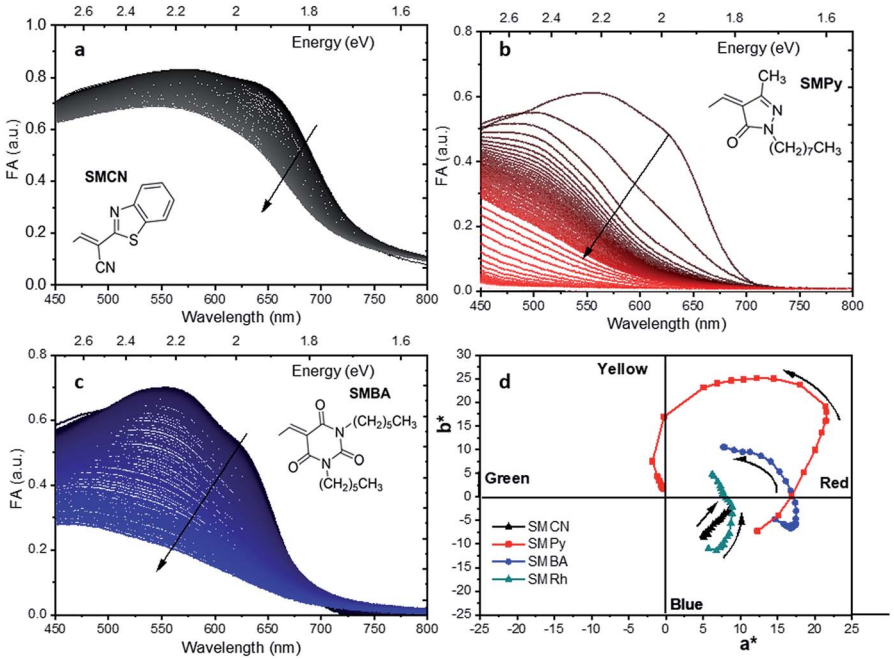

Fig. 4 UV-Vis absorptance (FA) spectra taken over a period of 11 days for (a) SMCN (b) SMPy and (c) SMBA. (d) CIE $L^*a^*b^*$ coordinate system representation of the UV-Vis for four molecules including SMRh.

Fig. 4d to describe the color as perceived by the human eye with a D65 standard illuminant. Briefly, in this coordinate system, L^* corresponds to lightness (contrast) while a^* and b^* are the green-red and blue-yellow color coordinates respectively.[43,44] The lightness values with time are given in Fig. S17.† In Fig. 4d, each of the films initially are a blue-purple in color, associated with transmission of blue and red regions of the electromagnetic spectrum. It is apparent that the relative fraction of photobleaching also corresponds to color coordinate shifts for the different molecules, a strong indication of variability in chemical degradation. SMPy shifts from the blue-red to the yellow-red quadrant before fully bleaching. SMBA shows a similar pattern with color quadrant changes but to a lesser extent. SMRh shows a loss in the purple color and moves from blue-red to yellow-red. The SMCN retains the initial color the best and is the only molecule that remains in the blue-red quadrant after 11 days ambient exposure.

Chemical degradation

The chemical mechanism of photooxidation is generally thought to proceed *via* a free-radical reaction as ascertained through EPR experiments described in the literature.[45–49] Traditionally, vibrational spectroscopies such as Raman or FTIR are used to provide a sense of the chemical alterations that occur within materials, as they provide a direct probe of chemical bonds. A similar experiment as the photobleaching described above was conducted using FTIR spectroscopy, with results provided in the ESI section.† We note that in order to obtain significant signal in the transmission mode configuration used here, thicker, drop-cast films were used. Given this, the sensitivity of the FTIR measurements to film changes was much slower relative to the optical photobleaching events. Furthermore, assigning definitive absorption peaks was difficult due to spectral congestion, particularly below 1800 cm^{-1}, but the FTIR results nevertheless provide complementary chemical information.

As an alternative to vibrational spectroscopy, X-ray photoelectron spectroscopy (XPS) provides chemical information at the elemental level and is the only technique that provides surface-sensitive information about the film on the local oxidation state of a particular atom (*i.e.* regions that are expected to degrade first). Fig. 5 shows the N 1s and S 2p core level spectra of the pristine and degraded films; here degradation was limited to only a 48 h exposure. O 1s and C 1s core level spectra are given in Fig. S22.† In Fig. 5a–c, the N 1s spectra allow for direct monitoring of the endcaps while the S 2p is predominantly reflective of the stability of the BDT-3T cores, with the exception of SMCN which has an additional sulfur component in the endcap. Table 1 provides the binding energies, full-width half maxima, and chemical assignment for each fitted peak of both the pristine and degraded films. For reference, the C and N K-edge and S L-edge XAS spectra of the degraded films can be found in Fig. S21.† A similar data set for small molecules mixed with PCBM can also be found in the ESI section (Fig. S24 and S25†).

Endcaps

Focusing first on SMPy (Fig. 5a), the pristine film has two contributions to the N 1s spectrum at 399.8 and 400.9 eV from the pyrazolone endcap, corresponding to the imine[50] (peak 1) and amide[51] (peak 2) nitrogen atoms, respectively, in a 1 : 1 ratio. After a 48 h photon dose, nearly complete loss of the

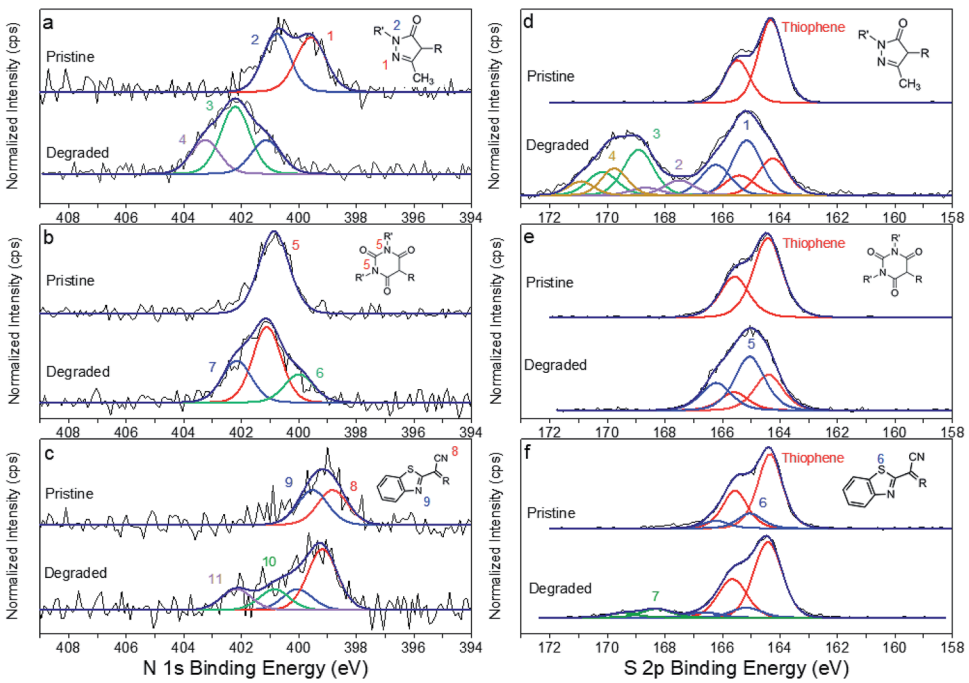

Fig. 5 N 1s and S 2p core level XPS spectra with peak fits for pristine and degraded (a, d) SMPy (b, e) SMBA (c, f) SMCN.

imine nitrogen is observed, indicating extensive oxidation chemistry. Concomitantly, two higher binding energy peaks at 402.2 and 403.2 eV emerge and a large amount of oxygen inclusion is observed in the film (25% increase, see Fig. S23†). We note that endcap degradation alone is insufficient to justify the +25% oxygen uptake, thereby implicating degradation of the BDT-3T core as discussed below.

Several mechanisms for singlet oxygen scavenging by pyrazolone derivatives have been reported for pyrazolone-based structures of interest to pharmaceutical[52] and dye[53–55] industries. Possible reaction pathways include a [4,2] Diels–Alder reaction to form quasi-ozone species[56–59] and/or a photochemical ring rearrangement.[60] The two additional, higher binding energy N 1s peaks are indicative of photorearrangement, which we suggest could occur *via* ring opening reactions resulting in functional groups such as carbonyls and nitrosos[61,62] or *N*-hydroperoxy[63] groups, most likely through reaction with singlet oxygen. The N K-edge in Fig. S21† corroborates this ring-opening hypothesis, with a complete change in the near-edge fine structure of the π^* regions. The formation of nitrosos and other NO_x species are confirmed in FT-IR spectra by appearance of peaks between 1650 and 1400 cm^{-1} (Fig. S18†). Extensive oxidation throughout the conjugated molecular structure is further supported by the observance of highly oxidized sulfur species in the S 2p XPS and oxidized carbon species in the C 1s XPS, discussed below, and the FTIR spectra in Fig. S11,† showing the emergence of sulfone, sulfoxide, and carbonyl species. The retention of some portions of the core suggest that the endcap may be the primary site of oxidative attack.

In Fig. 5b, pristine SMBA exhibits only a single peak at 400.8 eV, corresponding to the two electronically identical imide nitrogen atoms in the barbituric acid endcap. After 48 h of ambient light exposure, two new peaks emerge, one at lower binding energy (peak 6, 400.0 eV) and one at higher binding energy (peak 7, 402.2 eV). The majority of signal from the imide nitrogen (peak 5) is retained, however, indicating that only a fraction of the material has degraded. This behaviour is consistent with less photobleaching at shorter times (~2 days) for SMBA (Fig. S9†) than for SMPy. We suspect that the majority of film degradation occurs at the surface in the first 48 hours.

One hypothesis for the presence of a reduced N 1s environment is that photoexcitation promotes a delocalization of the excited state electron within one of the imide functional groups, which then undergoes ring opening with CO elimination. This would yield two new N 1s peaks: one species retaining its imide functionality (peak 7) and the other being reduced to a primary amide (peak 6).[64–66] FTIR spectroscopy (Fig. S19†) does not possess sufficient sensitivity to definitively verify this mechanism, which appears surface confined; however, we note subtle changes to the near-edge features of the N L-edge in Fig. S218.†

Fig. 5c shows the N 1s core spectra for SMCN, the most stable endcap of the three molecules studied. The pristine sample shows two N 1s peaks at 398.9 and 399.6 eV attributed to the nitrile and benzothiazole groups, respectively (peaks 8 and 9). Despite less pronounced photobleaching (Fig. 4a), the SMCN film exposed for 48 h under ambient illumination surprisingly shows clear evidence of degradation. The N 1s spectra of the degraded film exhibits a greatly reduced benzothiazole:nitrile N 1s ratio, going from 1 : 1 in the pristine films to 1 : 3 in the degraded film. Thus, we hypothesize that the resultant N 1s species associated with peaks 10 and 11 are due to benzothiazole decomposition. This assertion is corroborated by no change in the $\nu(C{\equiv}N)$ peak observed with this molecule in the corresponding FTIR spectra (Fig. S20†). Photochemical

Table 1 Chemical assignments to X-ray photoelectron spectroscopy peak fits in Fig. 5

Orbital	Molecule of origin	Assignment	Binding energy[a] [eV]	Width [eV]	Peak label
Nitrogen 1s	SMPy	Pyrazolone: imine	399.8 ± 0.1	1.19 ± 0.01	1
	SMPy	Pyrazolone: amide	400.9 ± 0.1	1.14 ± 0.045	2
	SMPy	Photorearranged amide	402.2 ± 0.1	1.18 ± 0.02	3
	SMPy	N═O	403.2 ± 0.1	1.15 ± 0.1	4
	SMBA	Barbituric acid	400.8 ± 0.1	1.2 ± 0.01	5
	SMBA		400.0 ± 0.1	1.17 ± 0.02	6
	SMBA		402.2 ± 0.1	1.17 ± 0.02	7
	SMCN	Nitrile	398.9 ± 0.1	1.19 ± 0.02	8
	SMCN	Benzothiazole	399.6 ± 0.1	1.19 ± 0.02	9
	SMCN		400.8 ± 0.1	1.2 ± 0.02	10
	SMCN		402.2 ± 0.1	1.19 ± 0.02	11
Sulfur 2p	SMCN, SMPy, SMBA	Thiophene	164.4 ± 0.1[b]	1.07 ± 0.08	
	SMPY	Thiophene$^{\delta+}$	165.3 ± 0.1	1.19 ± 0.02	1
	SMPy	Sulfoxide	167.6 ± 0.1	1.19 ± 0.02	2
	SMPy	Sulfinate ester	168.3 ± 0.1	1.2 ± 0.02	3
	SMPy	Sulfone	169.9 ± 0.1	1.04 ± 0.02	4
	SMBA	Thiophene$^{\delta+}$	165.1 ± 0.1	1.2 ± 0.02	5
	SMCN	Thiazole	165.1 ± 0.1	0.98 ± 0.01	6
	SMCN	SO_x	168.3 ± 0.1	1.19 ± 0.02	7

[a] Peaks were fit using 40% Gaussian 60% Lorentzian peak shapes. [b] Binding energy of S $2p_{3/2}$. Each S 2p doublet was fit to retain the necessary spin orbit splitting ratios by maintaining a constant peak separation 1.18 eV, a height ratio of 2 : 1 and equivalent full width half maximum.

incorporation of a hydroxide group with saturation of the imine bond[67] and radical cleavage[68] have been proposed reaction pathways in the literature, although the latter seems less likely due to steric hindrance effects. We note that the observed +9% oxygen incorporation cannot be explained by endcap degradation alone, as with SMPy. To understand this discrepancy, the chemistry of the BDT-3T core molecules must be understood.

BDT-3T core

Fig. 5d–f shows the S 2p spectra subjected to spectral decomposition for all three molecules, with the predominant signal arising from the BDT-3T core; SMCN has an additional contribution from the benzothiazole component of the endcap (Fig. 5f). The degradation of the BDT-3T core in all cases can be described by two main phenomena: (1) reduced, localized electron density on the sulfur (thiophene$^{\delta+}$) and (2) oxidation of the sulfur species to higher oxidation states.

In Fig. 5d, SMPy, in addition to showing the most extreme degradation both in optical spectroscopy and in endcap chemistry, also shows the greatest degradation of the BDT-3T core, consistent with electron density redistribution about the entire molecule. Peak 1 in Fig. 5d is attributed to partial oxidation of the thiophene ring (thiophene$^{\delta+}$), likely by charge transfer to the SMPy endcap to facilitate oxidative chemistry with O_2. Peaks 2 through 4 are hypothesized to be direct further oxidation of the S atoms to varying extents. Previous work on the photochemical degradation of poly(3-hexyl)thiophene (P3HT) has shown that thiophene groups are readily oxidized in ambient conditions to form sulfoxide (S=O), sulfinate ester, and sulfone species,[36,69] corresponding to peaks 2, 3 and 4 in Fig. 5d. At long exposure times, the FTIR data in Fig. S18† confirms the presence of sulfone and sulfoxide species between 1200 and 1000 cm^{-1}. Fig. S21† also shows a significant change in both the π^* and σ^* features of the degraded S L-edge. Furthermore, the appearance of peaks at 1715 and 1785 cm^{-1} in the infrared spectrum for the photo-oxidative degradation of SMPy (Fig. S18†) has also been seen before in the literature for the photo-oxidative degradation of P3HT.[36,69] These peaks have been attributed to the formation of various carbonyl groups at the hexyl side chains of the thiophene through a multistep oxygenation reaction instigated by an initial hydrogen abstraction from the alpha carbon in the chain. The formation of CO_x species is corroborated by the large high binding energy growth observed in C 1s XPS as well as the large degree of oxygen uptake as seen by the O 1s spectrum (Fig. S22†).

Relative to SMPY, SMBA (Fig. 5e) shows little evidence for direct sulfur oxidation and only a small presence of the thiophene$^{\delta+}$ feature at 165.1 eV, although the percent composition is greater than the unreacted BDT-3T contributions at the surface of the film. This observation suggests that SMBA ring opening with CO elimination does not lead to changes in bonding of the BDT-3T core. We hypothesize that this ring opening process alters the electron withdrawing nature of the endcap, giving rise to photobleaching of the chromophore, but allows retention of the BDT-3T structure.

The spectral data for SMCN does indicate direct sulfur oxidation upon degradation through the presence of a peak at 168.3 eV (peak 7, Fig. 5f), but to a significantly smaller extent than observed in SMPy. Interestingly, dominance of the spectral signature for thiophene$^{\delta+}$, observed with SMPy and SMBA, is not seen for SMCN. We do note a small reduction in the contribution from the benzothiazole sulfur, which implies the benzothiazole could be participating in formation of SO_x species, as supported by the N 1s spectrum of degraded SMCN (Fig. 5f). However, given that this molecule shows the greatest chromophore stability, the benzothiazole unit must not participate significantly in delocalization of the electron density across the molecule as supported by the DFT results in Fig. 1.

Incorporation of $PC_{71}BM$

The stabilizing effect of fullerene derivatives has been discussed in the literature with other types of semiconducting materials, namely polymeric semiconductors such as P3HT[70] and PPV.[71] It has been proposed that this general stabilization effect is due to the sub-ns quenching of the excited state induced in the semiconducting material, preventing subsequent intramolecular degradation mechanisms from occurring;[72] dynamics are controlled by the electron affinity of the fullerene.[15] More simply, creating faster electron transfer to the fullerene acceptor, relative to the rate of electron transfer to singlet oxygen, could decrease photo-degradation pathways.

While measuring rates of electron transfer are beyond the scope of this work, a qualitative analysis is still useful. Fig. S24† shows the same XPS results for 1 : 1 blended ratios of the organic small molecules with PCBM; the complementary figures for the X-ray absorption are given in Fig. S25.† With the exception of SMCN, we note that the fullerene incorporation decreases ambient photo-degradation. In addition to the possible mechanisms outlined above, this could possibly be due to changes in permeability of the film to ambient reactants,[73] such as H_2O or O_2, or possibly even the decrease of electron density on the semiconductor itself through a photo-induced electron transfer from the donor to the PCBM acceptor.[71,74] We note for the case of the highly reactive SMPy, the oxygenation of the thiophene is decreased and we observe the retention of the imine nitrogen peak. Similar behaviour is observed for SMBA. These hypotheses serve as motivation for future works.

Conclusions

Photobleaching of organic semiconductor materials is becoming a targeted topic as the field of OPV branches towards new technological developments where aesthetics are as or more important than power conversion efficiencies, such as building integrated photovoltaics and solar windows. Herein we considered the effect of endgroup substitution on the dynamics of photobleaching and mechanisms of photo-oxidation, independent of redox potential. This systematic study was afforded by computationally designing and then synthesizing three new push–pull small molecules following an A–D′–D–D′–A molecular design comprised of a BDT-3T core and

benzothiazoleacetonitrile, pyrazolone, or barbituric acid end-caps. By comparing across the molecule class, several key findings became apparent to guide new materials design. First, from SMPy, we concluded that the pyrazolone was the site of rapid free radical attack and such end groups should be avoided. More generally, a pertinent design rule we garnered from this end group is that systems that retain full pi-conjugation after free radical attack are prone to radical propagation throughout the molecule, direct oxygen incorporation, and rapid photobleaching. We suggest molecular design to focus on low reactivity and systems that once attacked, isolate the attack site from the core. This concept is further supported by comparison between SMCN and SMBA. For SMCN, our key finding is that the degradation chemistries do not necessarily coincide with photobleaching of the main absorptance features due to differences in electron delocalization. We emphasize these types of systems (*i.e.* SMCN) should be targets for color aesthetic applications. Alternatively, SMBA demonstrated less chemical degradation in ambient conditions, which is expected to lead to fewer trap states and retention in device efficiency, especially if encapsulated. Overall, our results speak to the importance of a thorough consideration of both electronic and chemical stability when designing new materials, with consideration of plausible degradation pathways based on chemical traits and not just on redox properties. Once stable molecules are identified, we hypothesize that generally, inclusion in blended heterojunctions should reduce degradation, although there are certainly exceptions to this rule. Future work should target kinetics of reactions and mechanistic pathways to further guide materials design.

Conflicts of interest

There are no conflicts to declare.

Acknowledgements

We express sincere gratitude to Dr Lieve Laurens at the NREL Spin Resonance Facility for assistance in collecting laser desorption ionization mass spectrometry data. A portion of this work is supported by the National Science Foundation under grant award DMR-1608289. MAA was supported by the National Science Foundation under grant award DGE-1735173. Use of the Stanford Synchrotron Radiation Lightsource, SLAC National Accelerator Laboratory, is supported by the U.S. Department of Energy, Office of Science, Office of Basic Energy Sciences under Contract No. DE-AC02-76SF00515. This work was authored in part by the National Renewable Energy Laboratory, operated by Alliance for Sustainable Energy, LLC, for the U.S. Department of Energy (DOE) under Contract No. DE-AC36-08GO28308. Funding provided by U.S. DOE Office of Energy Efficiency and Renewable Energy – Solar Energy Technologies Office. The views expressed in the article do not necessarily represent the views of the DOE or the U.S. Government. The U.S. Government retains and the publisher, by accepting the article for publication, acknowledges that the U.S. Government retains a nonexclusive, paid-up, irrevocable, worldwide license to publish or reproduce the published form of this work, or allow others to do so, for U.S. government purposes.

References

1 J. Yuan, Y. Zhang, L. Zhou, G. Zhang, H.-L. Yip, T.-K. Lau, X. Lu, C. Zhu, H. Peng, P. A. Johnson, M. Leclerc, Y. Cao, J. Ulanski, Y. Li and Y. Zou, *Joule*, 2019, **3**, 1140–1151.
2 X. Che, Y. Li, Y. Qu and S. R. Forrest, *Nat. Energy*, 2018, **3**, 422–427.
3 L. Meng, Y. Zhang, X. Wan, C. Li, X. Zhang, Y. Wang, X. Ke, Z. Xiao, L. Ding, R. Xia, H.-L. Yip, Y. Cao and Y. Chen, *Science*, 2018, **361**, 1094–1098.
4 T. Ameri, G. Dennler, C. Waldauf, H. Azimi, A. Seemann, K. Forberich, J. Hauch, M. Scharber, K. Hingerl and C. J. Brabec, *Adv. Funct. Mater.*, 2010, **20**, 1592–1598.
5 A. Colsmann, A. Puetz, A. Bauer, J. Hanisch, E. Ahlswede and U. Lemmer, *Adv. Energy Mater.*, 2011, **1**, 599–603.
6 C. J. M. Emmott, J. A. Röhr, M. Campoy-Quiles, T. Kirchartz, A. Urbina, N. J. Ekins-Daukes and J. Nelson, *Energy Environ. Sci.*, 2015, **8**, 1317–1328.
7 M. Manceau, E. Bundgaard, J. E. Carlé, O. Hagemann, M. Helgesen, R. Søndergaard, M. Jørgensen and F. C. Krebs, *J. Mater. Chem.*, 2011, **21**, 4132–4141.
8 A. Distler, T. Sauermann, H.-J. Egelhaaf, S. Rodman, D. Waller, K.-S. Cheon, M. Lee and D. M. Guldi, *Adv. Energy Mater.*, 2014, **4**, 1300693.
9 G. Li, R. Zhu and Y. Yang, *Nat. Photonics*, 2012, **6**, 153–161.
10 L. Y. Lu and L. P. Yu, *Adv. Mater.*, 2014, **26**, 4413–4430.
11 H. Yao, L. Ye, H. Zhang, S. Li, S. Zhang and J. Hou, *Chem. Rev.*, 2016, **116**, 7397–7457.
12 Y. Liang, Z. Xu, J. Xia, S.-T. Tsai, Y. Wu, G. Li, C. Ray and L. Yu, *Adv. Mater.*, 2010, **22**, E135–E138.
13 Z. He, C. Zhong, S. Su, M. Xu, H. Wu and Y. Cao, *Nat. Photonics*, 2012, **6**, 591–595.
14 J. Razzell-Hollis, J. Wade, W. C. Tsoi, Y. Soon, J. Durrant and J.-S. Kim, *J. Mater. Chem. A*, 2014, **2**, 20189–20195.
15 E. T. Hoke, I. T. Sachs-Quintana, M. T. Lloyd, I. Kauvar, W. R. Mateker, A. M. Nardes, C. H. Peters, N. Kopidakis and M. D. McGehee, *Adv. Energy Mater.*, 2012, **2**, 1351–1357.
16 S.-H. Liao, H.-J. Jhuo, Y.-S. Cheng and S.-A. Chen, *Adv. Mater.*, 2013, **25**, 4766–4771.
17 J. Kong, I.-W. Hwang and K. Lee, *Adv. Mater.*, 2014, **26**, 6275–6283.
18 G. J. Hedley, A. J. Ward, A. Alekseev, C. T. Howells, E. R. Martins, L. A. Serrano, G. Cooke, A. Ruseckas and I. D. W. Samuel, *Nat. Commun.*, 2013, **4**, 2867.
19 S. J. Lou, J. M. Szarko, T. Xu, L. P. Yu, T. J. Marks and L. X. Chen, *J. Am. Chem. Soc.*, 2011, **133**, 20661–20663.
20 B. J. T. de Villers, K. A. O'Hara, D. P. Ostrowski, P. H. Biddle, S. E. Shaheen, M. L. Chabinyc, D. C. Olson and N. Kopidakis, *Chem. Mater.*, 2016, **28**, 876–884.
21 Y. Z. Lin, Y. F. Li and X. W. Zhan, *Chem. Soc. Rev.*, 2012, **41**, 4245–4272.
22 A. Mishra and P. Bauerle, *Angew. Chem., Int. Ed.*, 2012, **51**, 2020–2067.
23 B. Walker, C. Kim and T. Q. Nguyen, *Chem. Mater.*, 2011, **23**, 470–482.

24 J. Zhou, X. Wan, Y. Liu, Y. Zuo, Z. Li, G. He, G. Long, W. Ni, C. Li, X. Su and Y. Chen, *J. Am. Chem. Soc.*, 2012, **134**, 16345–16351.
25 L. Dou, J. You, J. Yang, C.-C. Chen, Y. He, S. Murase, T. Moriarty, K. Emery, G. Li and Y. Yang, *Nat. Photonics*, 2012, **6**, 180–185.
26 L. Huo, S. Zhang, X. Guo, F. Xu, Y. Li and J. Hou, *Angew. Chem., Int. Ed.*, 2011, **50**, 9697–9702.
27 M. Wang, X. Hu, P. Liu, W. Li, X. Gong, F. Huang and Y. Cao, *J. Am. Chem. Soc.*, 2011, **133**, 9638–9641.
28 K. Sun, Z. Xiao, S. Lu, W. Zajaczkowski, W. Pisula, E. Hanssen, J. M. White, R. M. Williamson, J. Subbiah, J. Ouyang, A. B. Holmes, W. W. H. Wong and D. J. Jones, *Nat. Commun.*, 2015, **6**, 6013.
29 C. Vijay Kumar, L. Cabau, E. N. Koukaras, S. A. Siddiqui, G. D. Sharma and E. Palomares, *Nanoscale*, 2015, **7**, 7692–7703.
30 J. Zhou, Y. Zuo, X. Wan, G. Long, Q. Zhang, W. Ni, Y. Liu, Z. Li, G. He, C. Li, B. Kan, M. Li and Y. Chen, *J. Am. Chem. Soc.*, 2013, **135**, 8484–8487.
31 Y. S. Chen, X. J. Wan and G. K. Long, *Acc. Chem. Res.*, 2013, **46**, 2645–2655.
32 J. Min, C. Cui, T. Heumueller, S. Fladischer, X. Cheng, E. Spiecker, Y. Li and C. J. Brabec, *Adv. Energy Mater.*, 2016, **6**, 1600515.
33 B. Kan, Q. Zhang, M. M. Li, X. J. Wan, W. Ni, G. K. Long, Y. C. Wang, X. Yang, H. R. Feng and Y. S. Chen, *J. Am. Chem. Soc.*, 2014, **136**, 15529–15532.
34 L. E. Garner, V. Nellissery Viswanathan, D. H. Arias, C. P. Brook, S. T. Christensen, A. J. Ferguson, N. Kopidakis, B. W. Larson, Z. R. Owczarczyk, J. R. Pfeilsticker, P. C. Ramamurthy, S. H. Strauss, O. V. Boltalina and W. A. Braunecker, *J. Mater. Chem. A*, 2018, **6**, 4623–4628.
35 T. Heumueller, W. R. Mateker, I. T. Sachs-Quintana, K. Vandewal, J. A. Bartelt, T. M. Burke, T. Ameri, C. J. Brabec and M. D. McGehee, *Energy Environ. Sci.*, 2014, **7**, 2974–2980.
36 M. Manceau, A. Rivaton, J.-L. Gardette, S. Guillerez and N. Lemaître, *Polym. Degrad. Stab.*, 2009, **94**, 898–907.
37 G. W. T. M. J. Frisch, H. B. Schlegel, G. E. Scuseria, M. A. Robb, J. R. Cheeseman, G. Scalmani, V. Barone, G. A. Petersson, H. Nakatsuji, X. Li, M. Caricato, A. Marenich, J. Bloino, B. G. Janesko, R. Gomperts, B. Mennucci, H. P. Hratchian, J. V. Ortiz, A. F. Izmaylov, J. L. Sonnenberg, D. Williams-Young, F. Ding, F. Lipparini, F. Egidi, J. Goings, B. Peng, A. Petrone, T. Henderson, D. Ranasinghe, V. G. Zakrzewski, J. Gao, N. Rega, G. Zheng, W. Liang, M. Hada, M. Ehara, K. Toyota, R. Fukuda, J. Hasegawa, M. Ishida, T. Nakajima, Y. Honda, O. Kitao, H. Nakai, T. Vreven, K. Throssell, J. A. Montgomery Jr, J. E. Peralta, F. Ogliaro, M. Bearpark, J. J. Heyd, E. Brothers, K. N. Kudin, V. N. Staroverov, T. Keith, R. Kobayashi, J. Normand, K. Raghavachari, A. Rendell, J. C. Burant, S. S. Iyengar, J. Tomasi, M. Cossi, J. M. Millam, M. Klene, C. Adamo, R. Cammi, J. W. Ochterski, R. L. Martin, K. Morokuma, O. Farkas, J. B. Foresman, and D. J. Fox, *Gaussian 09, Revision A.02*, Gaussian, Inc., Wallingford CT, 2016.
38 Z. R. Owczarczyk, W. A. Braunecker, A. Garcia, R. Larsen, A. M. Nardes, N. Kopidakis, D. S. Ginley and D. C. Olson, *Macromolecules*, 2013, **46**, 1350–1360.
39 V. Nellissery Viswanathan, A. J. Ferguson, J. R. Pfeilsticker, B. W. Larson, L. E. Garner, C. P. Brook, S. H. Strauss, O. V. Boltalina, P. C. Ramamurthy and W. A. Braunecker, *Org. Electron.*, 2018, **62**, 685–694.
40 Z. B. Henson, G. C. Welch, T. van der Poll and G. C. Bazan, *J. Am. Chem. Soc.*, 2012, **134**, 3766–3779.
41 T. S. van der Poll, J. A. Love, T.-Q. Nguyen and G. C. Bazan, *Adv. Mater.*, 2012, **24**, 3646–3649.
42 G. C. Welch, L. A. Perez, C. V. Hoven, Y. Zhang, X.-D. Dang, A. Sharenko, M. F. Toney, E. J. Kramer, T.-Q. Nguyen and G. C. Bazan, *J. Mater. Chem.*, 2011, **21**, 12700–12709.
43 R. W. G. Hunt and M. Pointer, *Measuring Colour*, 4th edn, 2011.
44 C. J. Traverse, R. Pandey, M. C. Barr and R. R. Lunt, *Nat. Energy*, 2017, **2**, 849–860.
45 A. Aguirre, S. C. J. Meskers, R. A. J. Janssen and H. J. Egelhaaf, *Org. Electron.*, 2011, **12**, 1657–1662.
46 Y. Aoyama, T. Yamanari, T. N. Murakami, T. Nagamori, K. Marumoto, H. Tachikawa, J. Mizukado, H. Suda and Y. Yoshida, *Polym. J.*, 2014, **47**, 26.
47 L. Chen, S. Yamane, J. Mizukado, Y. Suzuki, S. Kutsuna, T. Uchimaru and H. Suda, *Chem. Phys. Lett.*, 2015, **624**, 87–92.
48 M. Havlicek, N. S. Sariciftci and M. C. Scharber, *J. Mater. Res.*, 2018, **33**, 1853–1859.
49 W. R. Mateker and M. D. McGehee, *Adv. Mater.*, 2017, **29**, 1603940.
50 S. Park, Y. Hu, J. O. Hwang, E.-S. Lee, L. B. Casabianca, W. Cai, J. R. Potts, H.-W. Ha, S. Chen, J. Oh, S. O. Kim, Y.-H. Kim, Y. Ishii and R. S. Ruoff, *Nat. Commun.*, 2012, **3**, 638.
51 G. Zorn, L.-H. Liu, L. Árnadóttir, H. Wang, L. J. Gamble, D. G. Castner and M. Yan, *J. Phys. Chem. C*, 2014, **118**, 376–383.
52 D. Costa, A. Gomes, J. L. F. C. Lima and E. Fernandes, *Redox Rep.*, 2008, **13**, 153–160.
53 N. Kuramoto, *J. Soc. Dyers Colour.*, 1990, **106**, 135–138.
54 C. K. Parmar, G. Rumbles and C. J. Winscom, *Phys. Chem. Chem. Phys.*, 2005, **7**, 1815–1823.
55 M. W. Rembold and H. E. A. Kramer, *Abstracts of Papers of the American Chemical Society*, 1980, **179**, 110-ORPL.
56 W. Adam and A. Rodriguez, *Tetrahedron Lett.*, 1981, **22**, 3509–3512.
57 M. Favier, R. Dewil, K. Van Eyck, A. Van Schepdael and D. Cabooter, *Chemosphere*, 2015, **136**, 32–41.
58 K. Gollnick and A. Griesbeck, *Tetrahedron*, 1985, **41**, 2057–2068.
59 A. G. Leach and K. N. Houk, *Chem. Commun.*, 2002, 1243–1255, DOI: 10.1039/b111251c.
60 S. N. Eğe, *J. Chem. Soc. C*, 1969, 2624–2630, DOI: 10.1039/j39690002624.

61 C. Castro, M. Dixon, I. Erden, P. Ergonenc, J. R. Keeffe and A. Sukhovitsky, *J. Org. Chem.*, 1989, **54**, 3732–3738.
62 S. Contarini, J. A. Schultz, S. Tachi, Y. S. Jo and J. W. Rabalais, *Appl. Surf. Sci.*, 1987, **28**, 291–301.
63 E. Friedrich, W. Lutz, H. Eichenauer and D. Enders, *Synthesis*, 1977, 893–894.
64 J. T. Bojarski, J. L. Mokrosz, H. J. Barton and M. H. Paluchowska, *Adv. Heterocycl. Chem.*, 1985, **38**, 229–297.
65 E. R. Garrett, J. T. Bojarski and G. J. Yakatan, *J. Pharm. Sci.*, 1971, **60**, 1145–1154.
66 J. M. Sayer and M. Depecol, *J. Am. Chem. Soc.*, 1977, **99**, 2665–2671.
67 E. Borowska, E. Felis and J. Kalka, *Chem. Eng. J.*, 2016, **304**, 852–863.
68 J. Miyazaki, H. Takiyama and M. Nakata, *RSC Adv.*, 2017, **7**, 4960–4974.
69 M. Manceau, J. Gaume, A. Rivaton, J.-L. Gardette, G. Monier and L. Bideux, *Thin Solid Films*, 2010, **518**, 7113–7118.
70 M. O. Reese, A. M. Nardes, B. L. Rupert, R. E. Larsen, D. C. Olson, M. T. Lloyd, S. E. Shaheen, D. S. Ginley, G. Rumbles and N. Kopidakis, *Adv. Funct. Mater.*, 2010, **20**, 3476–3483.
71 C. J. Brabec, G. Zerza, G. Cerullo, S. De Silvestri, S. Luzzati, J. C. Hummelen and S. Sariciftci, *Chem. Phys. Lett.*, 2001, **340**, 232–236.
72 H. Neugebauer, C. Brabec, J. C. Hummelen and N. S. Sariciftci, *Sol. Energy Mater. Sol. Cells*, 2000, **61**, 35–42.
73 C. W. T. Bulle-Lieuwma, W. J. H. van Gennip, J. K. J. van Duren, P. Jonkheijm, R. A. J. Janssen and J. W. Niemantsverdriet, *Appl. Surf. Sci.*, 2003, **203–204**, 547–550.
74 K. Vandewal, K. Tvingstedt, A. Gadisa, O. Inganäs and J. V. Manca, *Nat. Mater.*, 2009, **8**, 904.